Two-Photon Absorption in Monolayer MXenes

Gaozhong Wang†*, Daniel Bennett†, Chuanfang (John) Zhang†, Cormac Ó Coileáin, Meiying Liang, Niall McEvoy, Jing Jing Wang, Jun Wang, Kangpeng Wang*, Valeria Nicolosi and Werner J. Blau

Dr. G. Z. Wang, Dr. J. J. Wang and Prof. W. J. Blau

School of Physics, CRANN and AMBER, Trinity College Dublin, Dublin 2, Ireland

D. Bennett

Theory of Condensed Matter, Cavendish Laboratory, University of Cambridge, J. J. Thomson Avenue, Cambridge CB3 0HE, United Kingdom

Dr. C. Zhang, Dr. C. Ó Coileáin, M. Y. Liang, Dr. N. McEvoy and Prof. V. Nicolosi

School of Chemistry and AMBER, Trinity College Dublin, Dublin 2, Ireland

Prof. J. Wang

Laboratory of Micro-Nano Photonic and Optoelectronic Materials and Devices, Key Laboratory of Materials for High-Power Laser, Shanghai Institute of Optics and Fine Mechanics, Chinese 5Academy of Sciences, Shanghai 201800, P.R. China

Center of Materials Science and Optoelectronics Engineering, University of Chinese Academy of Sciences, Beijing 100049, P.R. China

Dr. K. P. Wang

Department of Electrical Engineering and Solid-State Institute, Technion-Israel Institute of Technology, Haifa 32000, Israel

† These authors contributed equally.

*Email: Gaozhong Wang, wangga@tcd.ie

Kangpeng Wang, kpwang@technion.ac.il

Keywords: Monolayer, MXenes, Two-Photon Absorption, Ultrafast Photonics, Nonlinear Optics

Abstract

Two-photon absorption (2PA) is a nonlinear optical (NLO) effect that typically occurs in a conventional semiconductor whose bandgap is larger than the energy of one excited photon but smaller than the energy of two photons. In this work, we report the experimental observation of strong 2PA in gapless MXene monolayers. This phenomenon was verified by a nonlinear transmission method and ultrafast dynamic studies based on a wavelength-degenerate, non-collinear pump-probe technique. We attribute the unconventional 2PA to the structures of the MXene energy bands near the Fermi level, which favors two-photon transitions and suppresses one-photon transitions due to parallel band absorption effects. These results, as well as the measured NLO parameters including the 2PA coefficient, absorption cross-section, excited carrier lifetimes, and third-order NLO susceptibility, provide a systematic understanding of the unusual NLO effect in MXenes and may be applied in advanced photonic and optoelectronic devices.

Light-matter interactions in two-dimensional (2D) materials have been in the spotlight of recent optics research because of the novel applications in nanoelectronics, valleytronics, photovoltaics and nanophotonics that they will potentially enable[1-7]. In the field of nonlinear optics (NLO), some 2D nanosheets, such as graphene and monolayer MoS_2, have been experimentally observed to exhibit strong two-photon absorption (2PA)[8-11]. This interesting NLO phenomenon has a wide range of applications in optical limiting, all-optical switching, logic[12], storage memory[13, 14], 3D lithography and printing[15]. 2PA is an NLO effect where an electron absorbs two photons simultaneously and is excited from the ground state via a virtual state. 2PA generally occurs when the gap between the ground and excited states is larger than the energy of one photon but smaller than the energy of two photons. Hence, one photon absorption (1PA) dominates when light interacts with a small bandgap semiconductor or gapless metal. Interestingly, 2PA instead of 1PA can be the dominant optical transition process in narrow bandgap materials under the right circumstances, but it is a challenge to experimentally observe this unusual optical phenomenon in bulk materials. This phenomenon, however, becomes possible in 2D materials thanks to their interesting electronic structures. Giant 2PA was reported in gapless bilayer graphene with four bands under the irradiation of 780 nm and 1100 nm photons[8]. This 2PA could happen because the two-photon transitions are enhanced due to the additional bands arising from the interlayer interactions in the bilayer system, which are absent from monolayer graphene. To date, bilayer graphene is the only gapless semi-metal in which the unconventional 2PA has been observed experimentally. The question remains whether or not

3

it is possible to observe 2PA in a material, which does not have a similar electronic structure to that of bilayer graphene or conventional semiconductors.

To address this issue, we performed NLO experiments on titanium carbide ($Ti_3C_2T_x$) monolayers, which belongs to the MXene family of 2D materials. MXenes are a class of wide-spectral photonic 2D materials with the chemical formula $M_{n+1}X_nT_x$, where M is an early transition metal, X is C and/or N, and T_x is the surface termination (=O, -OH or -F)[16, 17]. The broadband optical response of MXene makes them promising candidates for photonic devices such as saturable absorbers for mode-locking[18]. This wide-spectral response could lead to a new possible mechanism for 2PA in materials which have small energy gaps or are gapless.

In this paper, we demonstrate that strong 2PA in gapless MXene monolayers is indeed possible, using open-aperture Z-scan, time-resolved, wavelength-degenerate pump-probe measurements and first-principles calculations. We employed a size-selection technique to obtain dispersions of liquid-phase-exfoliated MXenes with two different flake sizes. The nonlinear optical extinction observed in the Z-scans was confirmed to be 2PA by the fitting of a second-order NLO absorption model and pump-probe results. Our results show that MXene monolayers possess a large 2PA coefficient and the two-photon excited carriers relax to the ground state via a tri-exponential decay process. The band structure and joint density of states (JDOS) from the first-principles calculations provide an explanation for the observation of two-photon transitions in the MXene. Our work offers a new insight into 2PA processes in 2D nanostructures and could be important for designing photonic devices.

Experimental Section

To prepare the delaminated MXene monolayers, we employed the minimally intensive layer delamination (MILD) method (see the Methods section)[19]. **Figure 1**a shows the typical image of the as-delaminated $Ti_3C_2T_x$ nanosheet prepared at 3500 rpm centrifugation speed by transmission electron microscopy. The MXene nanosheets possess a clean surface and a well-defined shape. The electron-transparent of the flakes indicates an ultrathin thickness. Figs. 1b-c show the statistical analysis of the nanosheets prepared at 3500 rpm centrifugation speed, suggesting a mean flake length of 448 ± 204 nm and a mean width of 282 ± 148 nm, which we refer as the large flakes. We define the distance along the longest direction as the length and the longest distance perpendicular to the length as the width. The sizes of our MXene nanosheets are similar to those obtained in previous reports[19]. For the sake of comparison, we also prepared MXene nanosheets at 12000 rpm centrifugation speed. Similar clean nanosheets were obtained with smaller size dimensions (see Fig. 1d), which we refer to as small flakes. According to the size histogram in Figs. 1 e-f (12000 rpm), the mean length and width decrease to 229 ± 119 nm and 134 ± 67 nm. Most of the few-layered laminates were removed after the centrifugation at 3500 rpm[20]. Consequently, the centrifugation speed directly influences the nanosheet size, but has limited effects on the thickness of the delaminated sheets. According to the atomic force microscopy (AFM) measurements in Fig. S4a, both large and small nanosheets possess an ultrathin morphology, with a monolayer thickness of ~1.5 nm obtained from the height profile (Fig. S4b)[21]. A statistical study **of the distribution of the** number of layers in the dispersions for large and small flake dispersions was carried out, see Fig. 1 g and h respectively. An **enhancement** in the percentage of monolayer was observed in the MXene dispersions obtained by centrifuging at 12,000 rpm in comparison to that at 3,500 rpm. This is consistent with the size-selectable technique **in** our previous report.[22, 23] The Raman spectra in Fig. 1i imply these

delaminated nanosheets are oxide-free, in which all of the characteristic MXene peaks can be seen.

The NLO response of the monolayer MXene was first studied using an open-aperture Z-scan set-ups based on a mode-locked Ti:Sapphire laser with a center wavelength of 800 nm with a pulse duration of ~100 fs and repetition rate of 100 kHz (Coherent RegA 9000) (see Methods). This technique is used to obtain the NLO properties of materials by measuring its optical transmission as a function of Z-axis position along the laser focused direction (see **Fig. 2**a). Figures 2c and d show the Z-scan results of the two MXene samples dispersed in deionized water with increasing incident excitation laser pulse energy from 100 nJ to 300 nJ. We observed the transmission dips near thein center of the Z-scan curves of both flake sizes, implying the nonlinear extinctions of the MXene dispersions. Because no NLO response was observed from the solvent (deionized water, see Supplementary Figure 1), we attributed such nonlinear extinctions to 2PA in the MXene flakes.

As the intensity of incident light, i.e. the incident photon population, increases two-photon optical transitions become possible (see Fig. 2b). This results in a decrease in the optical transmission when the sample is moved toward the focused point, as opposed to an increase when the sample is moved far away from the focused point in the Z-scan measurements.

To quantitatively analyze the 2PA properties of the MXenes, the Z-scan results were fitted using the standard NLO propagation equation[24]:

$$\frac{dI}{dz'} = -I \cdot (\alpha_0 + \beta I) \quad (1)$$

where z' is the propagation distance, I is the laser intensity at z', α_0 and β are the linear and nonlinear absorption coefficients, respectively. This NLO model provides a favorable fit to the entire set of Z-scan data obtained from 100 nJ to 300 nJ, shown using the solid lines in

Figs. 2c and d. The fitting parameters are listed in **Table 1**. There is a slight increase in the **fitted** nonlinear absorption coefficient as the laser energy increases, which could come from the nonlinear optical scattering and fitting errors. The nonlinear absorption coefficient β were found to be ~ $(0.89 \pm 0.20) \times 10^{-2}$ cm/GW for the small flakes and ~ $(1.20 \pm 0.20) \times 10^{-2}$ cm/GW for the large flakes. Size-dependent optical nonlinearity was reported in some 2D materials such as **black** phosphorus and transition metal dichalcogenide**s** (TMDs) [25, 26]. Saturable absorption was observed in large size flakes and reverse saturable absorption in small size samples[25]. This could be explained by the change in thickness and bandgap as the size changes. 2PA was observed in both our small and large size flakes and only **a** slight difference was seen in the 2PA coefficient as both are monolayer with the same band structure.

The positive values of β in Table 1 confirms the 2PA of the MXene monolayers at a central wavelength of 800 nm.

To further confirm the observed NLO extinction in Fig. 2 is a second order effect, the inverted normalized transmission $1/T_N$ of the MXene as a function of incident laser intensity is studied, as seen in **Fig. 3**. From the theory analysis (see Supplementary Note 1), if the nonlinear absorption is second-order effect, the inverted normalized transmission will be proportional to the laser intensity, that is

$$\frac{1}{T_N(I)} = 1 + \beta L I, \quad (2)$$

where L is the thickness of the NLO material. The experimental data in Fig. 3 shows a well linear trend and is fitted well to Eq. 2, suggesting the observed NLO extinction is indeed a second order effect.

The confirmation of the second-order NLO extinction in MXene helps to clarify the NLO mechanisms. It is known that the NLO extinction can be caused by nonlinear scattering, reverse saturable absorption and multi-photon absorption. We first exclude the nonlinear scattering because it is a thermal effect that depends on the formation of laser-induced micro-bubbles. Such micro-bubbles formations required a nanosecond timescale[27], but our pump-probe results (discussed later) suggest the NLO extinction emerges in around one picosecond. Reverse saturable absorption (RSA) is also unlikely to be the mechanism in MXene because RSA has high-order components larger than two[28], which will make the experimental data to be nonlinear in Fig. 3. The order of multi-photon absorption is dependent on how many photons are absorbed simultaneously. Therefore, two-photon absorption should be the only mechanism explaining the second-order NLO extinction observed in MXene in this work.

To study the errors of the pure 2PA model, a more general linear equation, $1/T_N (I_0)$ = a $+I_0 L\beta'$, was used to fit the experimental data as shown by the dashed lines in Fig. 3, which almost overlap with the solid lines. The fitting results are also summarized in Supplementary Table 1 for comparison. The errors of fitting the 2PA coefficient for the large and small MXene flakes are 5.75% and 0.60%, respectively, with corresponding errors of the fitting intercept of 0.17% and 0.03%, respectively, which are small enough to be neglected.

The second approach to obtain the NLO parameters from the normalized transmission is fitting the experimental results (**Fig. 4**) using the relationship:

$$T_N = \frac{ln(1+I_0 L\beta)}{I_0 L\beta}. \quad (3)$$

The derivation of this equation can be found in the supplementary information. The 2PA coefficients obtained by fitting the data using Eq. 3 for MXene monolayers were found to be

0.96×10^{-2} cm/GW and 1.39×10^{-2} cm/GW for large and small flakes, respectively. These results agree well with those using the NLO propagation equation (Eq. 1), as seen in Table 1. The 2PA coefficient of MXene is relatively small in comparison to that of some other 2D materials such as 2D **TMDs** , Bi_2Te_3 and graphene[11, 29, 30]. The 2PA coefficient (~0.2 cm/W) of graphene is enhanced by the excitonic Fano resonance at the saddle point[11]. Meanwhile, additional bands arising from the interlayer interactions in the bilayer graphene enhance the second-order extinction[8]. Once the 2PA coefficient is experimentally obtained, many optical parameters can be calculated to gain an insight into the NLO properties of monolayer MXene. The imaginary part of the third-order NLO susceptibility, $Im\chi^{(3)}$, connects to the nonlinear absorption coefficient β by

$$\Im\left\{\chi^{(3)}\right\} = \frac{10^{-7}c\lambda n^2}{96\pi^2}\beta, \quad (4)$$

where c is the speed of light, λ is the laser center wavelength and n is the refractive index, which is ~2.65 for the MXene flakes at the center wavelength of 800 nm [31]. The values of $Im\chi^{(3)}$ for the large and small flake sizes were found to be 2.14×10^{-14} and 1.58×10^{-14} esu respectively, which are about one order of magnitude larger than those of 2D molybdenum disulfide (~10^{-15} esu)[32]. To eliminate the discrepancy resulting from the linear absorption (α_0), the figure of merit, FOM= $|Im\chi^{(3)}/\alpha_0|$, is defined for characterizing the optical nonlinearity of the sample with different concentrations. The FOM for the MXene flakes are of the order of magnitude of 10^{-15} esu·cm.

The 2PA cross-section of monolayer MXene at a wavelength of λ, $\sigma(\lambda)$, is given by[10]

$$\sigma(\lambda) = \frac{\beta hc}{N\lambda}, \quad (5)$$

where h is Planck's constant and $N = 3.1 \times 10^{22}$ cm^{-3} is the molecule density[33]. According to Eq. 5, the 2PA cross-sections of the MXene flakes were calculated to be ~10^{-2} GM/(photon·molecule), where GM =10^{-50} cm^{4}s stands for Göppert-Maye[34].

The ultrafast dynamics of the 2PA in the MXene monolayers was investigated using a time-resolved, wavelength-degenerate pump-probe experiment (**Fig. 5**a, see Methods for more details). In a pump-probe measurement of 2PA, one electron is excited by absorbing two photons of the pump beam, and the excited electrons are subsequently detected by obtaining the differential transmission of the probe beam, $\Delta T/T$: the relative change of the probe beam transmission with and without the pump beam. This differential transmission is defined as $\Delta T/T = (T_p - T_0)/T_0$, where T_0 and T_p represent the transmission of the probe light without and with the presence of the pump pulses, respectively. It is measured as a function of the pump-probe delay time to resolve the excitation carrier dynamics. The schematic of this optical setup is illustrated in Fig. 5a and additional details can be found in the methods section. Figures 5b–c show the transient absorption curves of the large and small flake samples a function of the pump-probe delay time at various pump powers from 5 mW to 25 mW. At the zero delay time, we observed strong photoinduced absorption, *i.e.*, negative $\Delta T/T$. Such photoinduced absorption originates from 2PA: the high intensity of pump pulse could excite the free carriers and those carriers increase the optical absorption which were detected by the probe pules. This photoinduced absorption reaches its maximum at ~ 100 fs and diminishes within ~1 ps. Then a small photoinduced bleaching (positive $\Delta T/T$) was observed after 1 ps delayed time, which may be induced by the bandgap renormalization[35]. Finally, the excited carriers recombined and the differential transmission $\Delta T/T$ recover to zero.

To obtain the timescales of those processes, a tri-exponential model with autocorrelation that contains one negative part and two positive parts is used to fit the experimental differential transmission ($\Delta T/T$) as a function of delay time[3, 36]

$$\frac{\Delta T}{T} = -D_1 exp\left(\frac{-t}{\tau_1}\right) erfc\left(\frac{\delta}{\sqrt{2}\tau_1} - \frac{t}{\sqrt{2}\delta}\right) + D_2 exp\left(\frac{-t}{\tau_2}\right) erfc\left(\frac{\delta}{\sqrt{2}\tau_2} - \frac{t}{\sqrt{2}\delta}\right) +$$

$$D_3 exp\left(\frac{-t}{\tau_3}\right) erfc\left(\frac{\delta}{\sqrt{2}\tau_3} - \frac{t}{\sqrt{2}\delta}\right), \quad (6)$$

where t is the pump-probe delay time, δ is the laser pulse duration and '$erfc$' is the complementary error function. τ_1 is the relaxation time related to the negative $\Delta T/T$, and τ_2 and τ_3 are the relaxation times related to the positive $\Delta T/T$. D_1, D_2 and D_3 are the corresponding amplitudes. The fitted curves are shown in Fig. 5b and c as solid lines, which are in well agreements with the experimental results. The fitted lifetimes are summarized in **Table 2**, where we attributed τ_1, τ_2 and τ_3 to the lifetime of the 2PA induced free carriers, the bandgap renormalization and electron-hole recombination, respectively. We found the 2PA induced free carriers in MXene have a lifetime around 110–130 fs.

It is very surprising to observe strong 2PA in a gapless 2D material. In order to obtain an insight into these unconventional observations, we calculated the band structure and joint density of states (JDOS) using first principles calculations (see the Methods section). The band structure is shown in **Fig. 6**a. Unlike in the reference[37], where it was suggested that the Ti_3C_2 monolayers undergo a metal to semiconducting transition after surface termination by OH or F, we found that the monolayers were still metallic after termination. However, a careful first-principles study has suggested that the monolayers can either be a metal or narrow gap semiconductor depending on the stacking of the terminations on the surfaces[38]. We can see from the band structure that there is a gap of roughly twice the photon energy near the M point in the Brillouin zone (BZ), around which the bands above and below the

Fermi level are relatively flat with respect to one another. The gaps which roughly correspond to the one-photon energy occur near the K point, where the bands have a steep Dirac-cone-like shape. We can see in Fig. 6b that this results in a dip in the JDOS at the one-photon energy and a peak at twice the photon energy.

Monolayer MXene $Ti_3C_2T_x$ (T = F or OH) is a gapless material in which we observed 2PA using 1.55 eV photons. First-principles calculations provide an explanation for why the 2PA is strong and the 1PA is suppressed. While single-photon transitions are governed by Fermi's golden rule, the Hamiltonian matrix elements between initial and final states times the JDOS at that energy difference, the two-photon case is a nonlinear phenomenon and therefore must be described using second order perturbation theory[39]. Since 2PA is a second-order effect, any situation in which it is the primary mechanism for excitations, as is the case here, would appear surprising and unlikely. This is especially true for monolayer graphene, for example; in bilayer graphene there are more bands around the Fermi level and thus more two-photon transitions available[8]. In our case we attribute the 2PA in the MXene monolayers to the shape of the bands near the Fermi level of $Ti_3C_2(OH)_2$, which favours two-photon transitions and not one-photon transitions due to parallel band absorption effects[40].

The band structure calculations in Fig. 6a show that the one photon energy, ~1.5 eV, occurs at points in the Brillouin zone (BZ) where the bands have a steep conic-like shape. The bands are steep with respect to one another, and thus there will not be many transitions at this energy contributing to the JDOS. In contrast, the bands at twice the photon energy are flatter. This could explain both the strong 2PA as well as the suppressed 1PA at this energy. The JDOS calculation in Fig. 6b shows that there is a peak at 2.96 eV, which corresponds to the energy of two photons. This plot of the JDOS, together with the band structure calculations,

supports the experimental observation of strong 2PA. The calculations presented in Fig. 6 support the parallel band effects that lead to strong 2PA in these MXene monolayers.

In summary, we have experimentally observed unconventional 2PA in gapless MXene $Ti_3C_2T_x$ (T=F or OH) monolayers with support from nonlinear optical measurements and first-principles calculations. The experiments were based on a pulse laser with duration of ~100 fs, center wavelength of 800 nm and repetition of 100 kHz. Our Z-scan results suggested the 2PA coefficient and absorptive cross-section of MXene are as large as 1.2×10^{-2} cm/GW and 0.96×10^{-2} GW for large flakes, and 0.89×10^{-2} cm/GW and 0.67×10^{-2} GW for small flakes. This unconventional 2PA behavior was confirmed by analysis using a second-order NLO absorption model as well as ultrafast dynamics. The lifetimes of the free carriers excited by 2PA were measured to be ~110–130 fs. The JDOS together with the band structure calculations provide convincing support for the experimental observation of strong 2PA. This study is important for the understanding of 2PA in 2D materials beyond bilayer graphene and could lead to the observation of 2PA in other 2D materials as well as applications for photonics devices.

Materials and Methods

Preparation of MXene monolayers: Deionized water was added to m-$Ti_3C_2T_x$ (m stands for multilayer), followed by vigorously shaking for 5 min. This process delaminates the m-$Ti_3C_2T_x$ into single- or few-layered nanosheets well dispersed in water. After that, the mixture was centrifuged at 3500 rpm for 30 min and the top 80% supernatant was collected as the large MXene flakes (3500 rpm dispersion). To obtain the small MXene flakes (12000 rpm MXene dispersion), we furtherly centrifuged the large flake dispersions at 12000 rpm for 1 h. The dispersions were contained in 1 mm cuvettes for characterization.

Characterizations: AFM height maps of the exfoliated flakes, drop-cast onto SiO_2/Si substrates, were acquired with a Bruker Multimode 8 in peak-force tapping mode using Scanasyst-Air probes. Fresh MXene solutions were drop-cast onto ultra-thin carbon film TEM grids. After the evaporation of water, the grids were transferred to a glove box overnight. The morphology of the delaminated MXene flakes and their size dimensions were studied by a FEI Titan 80-300S/TEM.

Open-aperture Z-scan: The schematic diagram of our Z-scan setup is showed in Fig. 2a. The purpose of the open-aperture Z-scan is to achieve NLO information via the measurement of optical transmission as a function of incident light intensity. The incident intensity is varied by moving the sample along a focused laser beam, *i.e.,* Z-axis direction. The femtosecond laser (Coherent RegA 9000) was chopped at 1300 Hz and its transmitted light that passed through the sample was collected by a photodiode. In the meantime, a small portion of the laser beam was split as the reference signal, which was modulated by an optical chopper at 700 Hz and incident into the same photodiode (Thorlabs SM1PD1B). The signals of the transmitted and reference beam are extracted by a dual-channel lock-in amplifier. Then the optical transmission can be obtained from dividing the transmitted signal to the reference one. The linear optical absorption coefficients of the samples, α_0, were obtained from the measurements at a low laser intensity (Supplementary Figure 2) using the Beer-Lambert law.

Pump-probe*:* We employed a wavelength-degenerate and non-collinear pump-probe setup as in Fig. 5a, based on 800 nm, 100 fs and 100 kHz laser pulses. The laser was split into a low-intensity beam for probing and a relatively intense one for pumping. The two beams were modulated by a single optical chopper at frequencies of 442 Hz and 733 Hz respectively. The use of a single optical chopper can maintain the phase relationship between two beams, which is important for the final signal extraction. To eliminate coherent artefacts,

a half-wave plate was used to rotate the polarization of the probe light by 90 degrees. The probe beam was delayed by a 150 mm linear translation stage with integrated controller (Thorlabs LTS150/M). The minimum achievable incremental movement of the stage is 0.1 µm (0.33 fs) and so the time resolution of our setup is limited by the laser pulse duration. The optical signal is measured by a silicon photodiode (Thorlabs SM1PD1B). To obtain the differential transmission, we measured the amplitude of the sum frequency (1175 Hz) of pump and probe beams by a lock-in amplifier.

First-principles Calculations: The electronic properties of MXene monolayers were studied by density function theory (DFT). Geometry relaxations and band structure were calculated using the SIESTA package, which employs numerical atomic orbitals[41]. All calculations were performed within the generalised gradient approximation (GGA) using the PBEsol exchange-correlation functional[42]. Norm-conserving Troullier-Martin pseudopotentials were used to replace the core electrons[43]. A Fermi-Dirac distribution with a temperature of 0.075 eV was used to smear the occupancy of the one-particle electronic states. Reciprocal space integrations were performed on a Monkhorst-Pack k-point mesh[44]. A mesh cutoff energy of 1000 eV and a k-point mesh of $10 \times 10 \times 1$ were found to be sufficient to converge the lattice constants of monolayers with different surface terminations. A finer mesh of $100 \times 100 \times 10$ was used when calculating optical transitions in the Brillouin zone.

The crystal structure of the monolayers were obtained following a similar method to the one described in the reference[37]. Starting with the structure of bulk $Ti_3Al_2C_2$ [45], the Ti_3C_2 layers were separated by a distance of roughly 50 Å, then the Al termination was replaced by an OH or F termination on either side of the monolayer. A dipole correction was introduced in the vacuum region in order to prevent long-range interactions between the monolayers and their periodic images. From geometry relaxation calculations, lattice constants of 3.12 Å and

2.97 Å were found for monolayers with OH and F terminations, respectively, in good agreement with those obtained in the reference[37]. The relaxed structure was found from the geometry relaxation, using the conjugate gradient method. Keeping the in-plane components of atomic positions fixed to preserve the symmetries of the monolayers, the out-of-plane coordinates were relaxed until the total forces on all atoms were less than 10 meV/Å. Having the relaxed crystal structures, the band structures were obtained along the high-symmetry directions in the Brillouin zone (BZ).

Optical transitions were studied using CASTEP[46], a plane-wave DFT program[47] and OptaDOS[48], a post-processing program, using the same parameters as those used in the SIESTA calculations. The structural and energetic results from both DFT codes agree well. The vertical optical transitions were calculated using OptaDOS. The JDOS was calculated with 10 eV energy difference, 0.01 eV spacing and 0.4 eV adaptive smearing[49].

Acknowledgements

Conflict of interest

There is no conflict of interest.

References

1. Sie, E.J., et al., *Large, valley-exclusive Bloch-Siegert shift in monolayer WS$_2$.* Science, 2017. **355**(6329): p. 1066-1069.
2. Ye, Z., D. Sun, and T.F. Heinz, *Optical manipulation of valley pseudospin.* Nature physics, 2017. **13**(1): p. 26-29.

3.   Wang, G., et al., *Ultrafast Nonlinear Optical Properties of a Graphene Saturable Mirror in the 2 μm Wavelength Region.* Laser & Photonics Reviews, 2017. **11**(5): p. 1700166-1700175.

4.   Wang, G., et al., *Tunable nonlinear refractive index of two-dimensional MoS₂, WS₂, and MoSe₂ nanosheet dispersions.* Photonics Research, 2015. **3**(2): p. A51-A55.

5.   Wang, G., et al., *Tunable effective nonlinear refractive index of graphene dispersions during the distortion of spatial self-phase modulation.* Applied Physics Letters, 2014. **104**(14): p. 141909.

6.   Lu, L., et al., *Few-layer bismuthene: sonochemical exfoliation, nonlinear optics and applications for ultrafast photonics with enhanced stability.* Laser & Photonics Reviews, 2018. **12**(1): p. 1700221.

7.   Ma, J., et al., *Few-layer black phosphorus based saturable absorber mirror for pulsed solid-state lasers.* Optics express, 2015. **23**(17): p. 22643-22648.

8.   Yang, H., et al., *Giant two-photon absorption in bilayer graphene.* Nano letters, 2011. **11**(7): p. 2622-2627.

9.   Zhang, S., et al., *Direct observation of degenerate two-photon absorption and its saturation in WS₂ and MoS₂ monolayer and few-layer films.* ACS nano, 2015. **9**(7): p. 7142-7150.

10.   Li, Y., et al., *Giant two-photon absorption in monolayer MoS2.* Laser & Photonics Reviews, 2015. **9**(4): p. 427-434.

11.   Chen, W., Y. Wang, and W. Ji, *Two-photon absorption in graphene enhanced by the excitonic fano resonance.* The Journal of Physical Chemistry C, 2015. **119**(29): p. 16954-16961.

12.   Hayat, A., et al., *Applications of two-photon processes in semiconductor photonic devices: invited review.* Semiconductor Science and Technology, 2011. **26**(8): p. 083001.

13.   Parthenopoulos, D.A. and P.M. Rentzepis, *Three-dimensional optical storage memory.* Science, 1989. **245**(4920): p. 843-845.

14.   Cumpston, B.H., et al., *Two-photon polymerization initiators for three-dimensional optical data storage and microfabrication.* Nature, 1999. **398**(6722): p. 51.

15.   Infuehr, R., et al., *Functional polymers by two-photon 3D lithography.* 2007. **254**(4): p. 836-840.

16.   Lukatskaya, M.R., et al., *Cation intercalation and high volumetric capacitance of two-dimensional titanium carbide.* Science, 2013. **341**(6153): p. 1502-1505.

17.   Jiang, X., et al., *Broadband Nonlinear Photonics in Few-Layer MXene Ti3C2Tx (T= F, O, or OH).* Laser & Photonics Reviews: p. 1700229.

18.   Jhon, Y.I., et al., *Metallic MXene Saturable Absorber for Femtosecond Mode-Locked Lasers.* Advanced Materials, 2017. **29**(40).

19.   Lipatov, A., et al., *Effect of synthesis on quality, electronic properties and environmental stability of individual monolayer Ti3C2 MXene flakes.* 2016. **2**(12): p. 1600255.

20.   Alhabeb, M., et al., *Guidelines for Synthesis and Processing of Two-Dimensional Titanium Carbide (Ti₃C₂Tₓ MXene).* 2017. **29**(18): p. 7633-7644.

21.   Zhang, C.J., et al., *High capacity silicon anodes enabled by MXene viscous aqueous ink.* 2019. **10**(1): p. 849.

22.   Backes, C., et al., *Production of Highly Monolayer Enriched Dispersions of Liquid-Exfoliated Nanosheets by Liquid Cascade Centrifugation.* ACS nano, 2016.

23.   Zhang, C.J., et al., *High capacity silicon anodes enabled by MXene viscous aqueous ink.* Nature communications, 2019. **10**(1): p. 849.

24.   Sheik-Bahae, M., et al., *Sensitive measurement of optical nonlinearities using a single beam.* IEEE journal of quantum electronics, 1990. **26**(4): p. 760-769.

25.   Zhou, K.G., et al., *Size-Dependent Nonlinear Optical Properties of Atomically Thin Transition Metal Dichalcogenide Nanosheets.* Small, 2015. **11**(6): p. 694-701.

26.   Zhang, S., et al., *Size-dependent saturable absorption and mode-locking of dispersed black phosphorus nanosheets.* Optical Materials Express, 2016. **6**(10): p. 3159-3168.

27.   Wang, J., et al., *Broadband nonlinear optical response of graphene dispersions.* Advanced Materials, 2009. **21**(23): p. 2430-2435.

28.   O'Flaherty, S.M., et al., *Molecular engineering of peripherally and axially modified phthalocyanines for optical limiting and nonlinear optics.* Advanced materials, 2003. **15**(1): p. 19-32.

29.   Qiao, J., et al., *Two-photon absorption within layered Bi_2Te_3 topological insulators and the role of nonlinear transmittance therein.* Journal of Materials Chemistry C, 2019. **7**(23): p. 7027-7034.

30.   Zhou, F., et al., *Two-photon absorption arises from two-dimensional excitons.* Optics Express, 2018. **26**(13): p. 16093-16101.

31.   Miranda, A., et al., *Rendering Ti_3C_2Tx (MXene) monolayers visible.* Materials Research Letters, 2017. **5**(5): p. 322-328.

32.   Wang, K., et al., *Ultrafast saturable absorption of two-dimensional MoS_2 nanosheets.* ACS nano, 2013. **7**(10): p. 9260-9267.

33.   Chaudhuri, K., et al., *Highly Broadband Absorber Using Plasmonic Titanium Carbide (MXene).* ACS Photonics, 2018.

34.   He, G.S., et al., *Multiphoton absorbing materials: molecular designs, characterizations, and applications.* Chemical reviews, 2008. **108**(4): p. 1245-1330.

35.   Wang, G., et al., *Ultrafast Carrier Dynamics and Bandgap Renormalization in Layered $PtSe_2$.* Small, 2019. **15**: p. 1902728.

36.   Wang, K., et al., *Ultrafast Nonlinear Excitation Dynamics of Black Phosphorus Nanosheets from Visible to Mid-Infrared.* ACS nano, 2016: p. 6923-6932.

37.   Naguib, M., et al., *Two-dimensional nanocrystals produced by exfoliation of Ti_3AlC_2.* Advanced Materials, 2011. **23**(37): p. 4248-4253.

38.   Tang, Q., Z. Zhou, and P. Shen, *Are MXenes promising anode materials for Li ion batteries? Computational studies on electronic properties and Li storage capability of Ti_3C_2 and $Ti_3C_2X_2$ (X= F, OH) monolayer.* Journal of the American Chemical Society, 2012. **134**(40): p. 16909-16916.

39.   Attaccalite, C., et al., *Two-photon absorption in two-dimensional materials: The case of hexagonal boron nitride.* Physical Review B, 2018. **98**(16): p. 165126.

40.   Harrison, W.A., *Parallel-band effects in interband optical absorption.* Physical Review, 1966. **147**(2): p. 467.

41.   Soler, J.M., et al., *The SIESTA method for ab initio order-N materials simulation.* Journal of Physics: Condensed Matter, 2002. **14**(11): p. 2745.

42.   Perdew, J.P., et al., *Restoring the density-gradient expansion for exchange in solids and surfaces.* Physical review letters, 2008. **100**(13): p. 136406.

43.   Troullier, N. and J.L. Martins, *Efficient pseudopotentials for plane-wave calculations.* Physical review B, 1991. **43**(3): p. 1993.

44.   Monkhorst, H.J. and J.D. Pack, *Special points for Brillouin-zone integrations.* Physical review B, 1976. **13**(12): p. 5188.

45.   Zhou, Y., et al., *Electronic and structural properties of the layered ternary carbide Ti_3AlC_2.* Journal of Materials Chemistry, 2001. **11**(9): p. 2335-2339.

46.   Clark, S.J., et al., *First principles methods using CASTEP.* Zeitschrift für Kristallographie-Crystalline Materials, 2005. **220**(5/6): p. 567-570.

47.   Nicholls, R., et al. *OptaDOS-a new tool for EELS calculations.* in *Journal of Physics: Conference Series*. 2012. IOP Publishing.

48.   Morris, A.J., et al., *OptaDOS: A tool for obtaining density of states, core-level and optical spectra from electronic structure codes.* Computer Physics Communications, 2014. **185**(5): p. 1477-1485.

49.   Yates, J.R., et al., *Spectral and Fermi surface properties from Wannier interpolation.* Physical Review B, 2007. **75**(19): p. 195121.
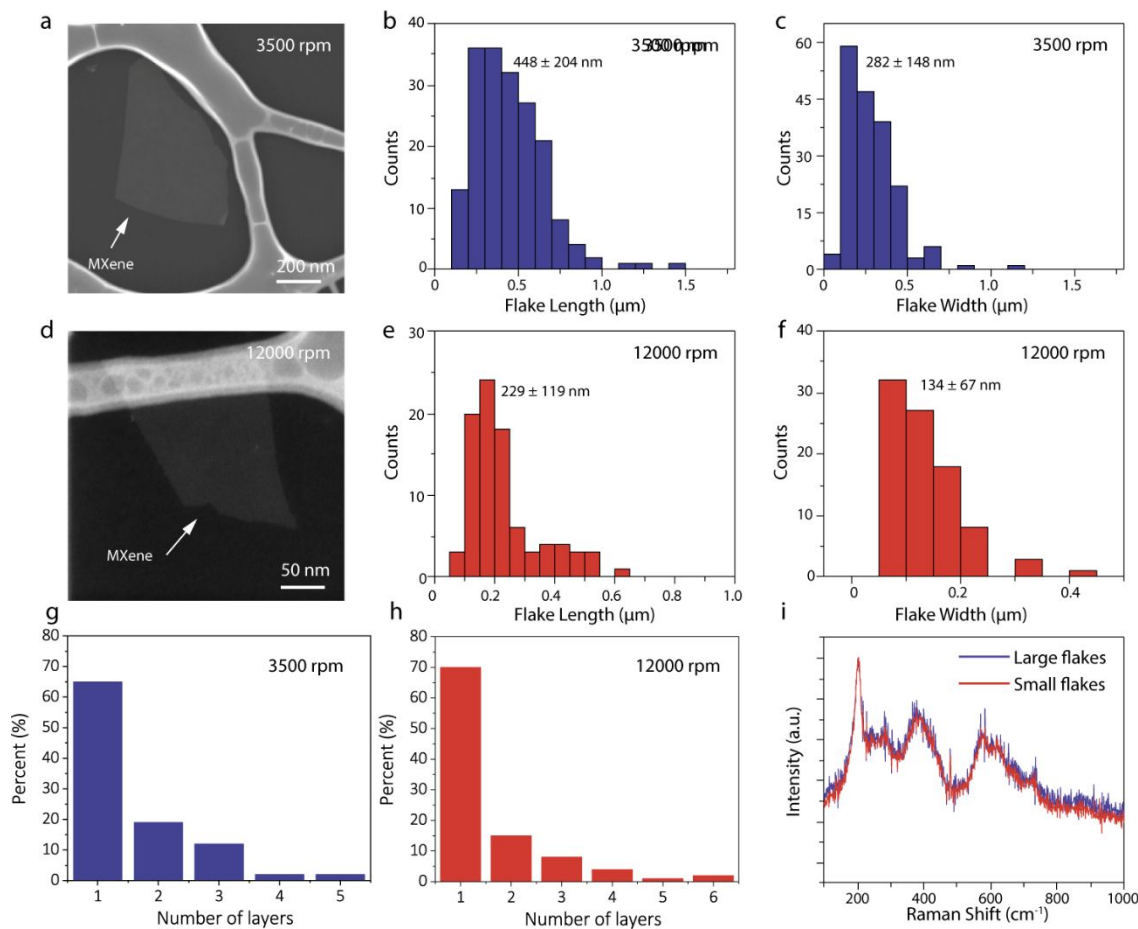
Figure 1 | Characterizations of the MXene monolayers ($Ti_3C_2T_x$, T = F or OH). a, transmission electron microscopy (TEM) image of a MXene flake obtained by centrifuging at 3500 rpm. **b-c,** Length (b) and (c) length histograms of MXene flakes (obtained by centrifuging at 3500 rpm) determined by statistical analysis. **d,** TEM image of a MXene flake obtained by centrifuging at 12,000 rpm. **e-f,** Length (e) and (f) length histograms of the MXene flakes centrifuged at 12,000 rpm determined by statistical analysis. **g-h**, **Distribution of the number of layers** in large and small MXene flake dispersions. **i,** Raman spectra of the MXene flakes with large and small sizes.
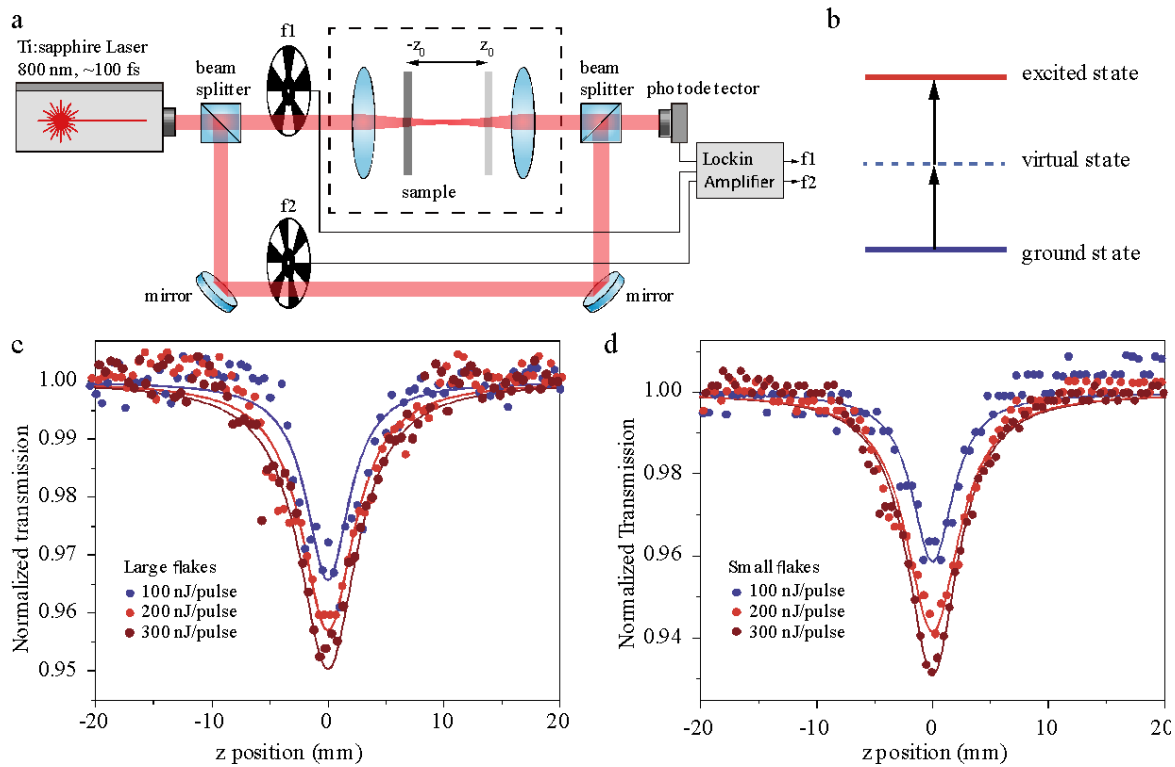
Figure 2 | Nonlinear optical measurements of MXene flakes. a, schematics of the Z-scan setup. **b**, the mechanism diagram of two-photon absorption (2PA). **c-d,** the experimental z-scan results of the (**c**) large and (**d**) small flakes. The dip in the Z-scan curves imply the 2PA responses of the MXene. Solid lines are fitted results.
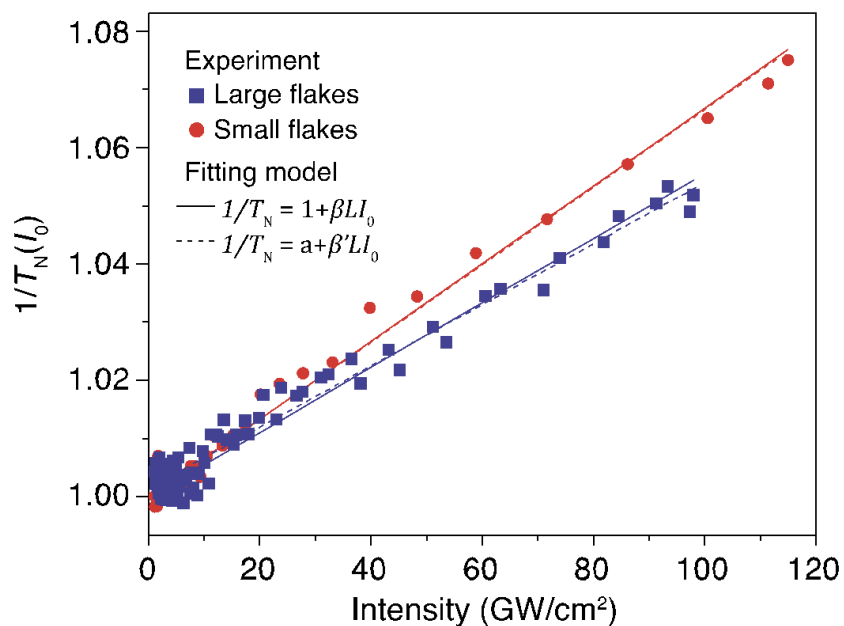

Figure 3 | The inverted normalized optical transmission of the MXene monolayers as a function of incident intensity. Solid lines are the fitting results using a linear model as Eq. 2.

The strong linearity of the inverted normalized transmission implies that the NLO extinction in MXene is a second-order effect.
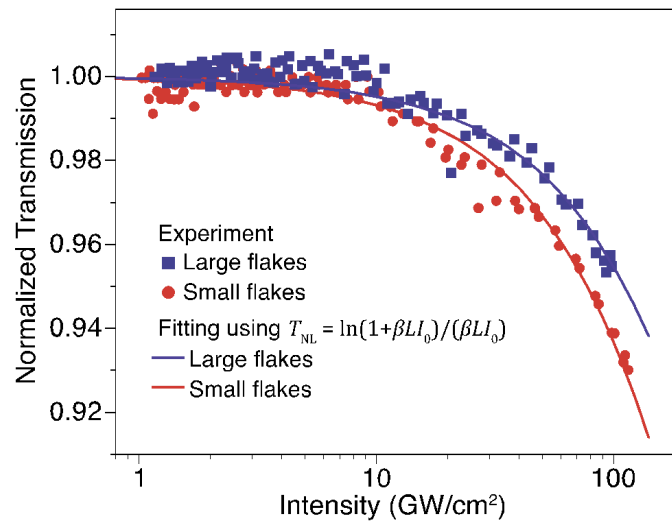

Figure 4 | Normalized optical transmission of the MXene monolayers as a function of incident intensity. The two-photon absorption coefficients of large flakes and small flake MXene were fitted to be 0.96×10^{-2} cm/GW and 1.39×10^{-2} cm/GW, respectively.
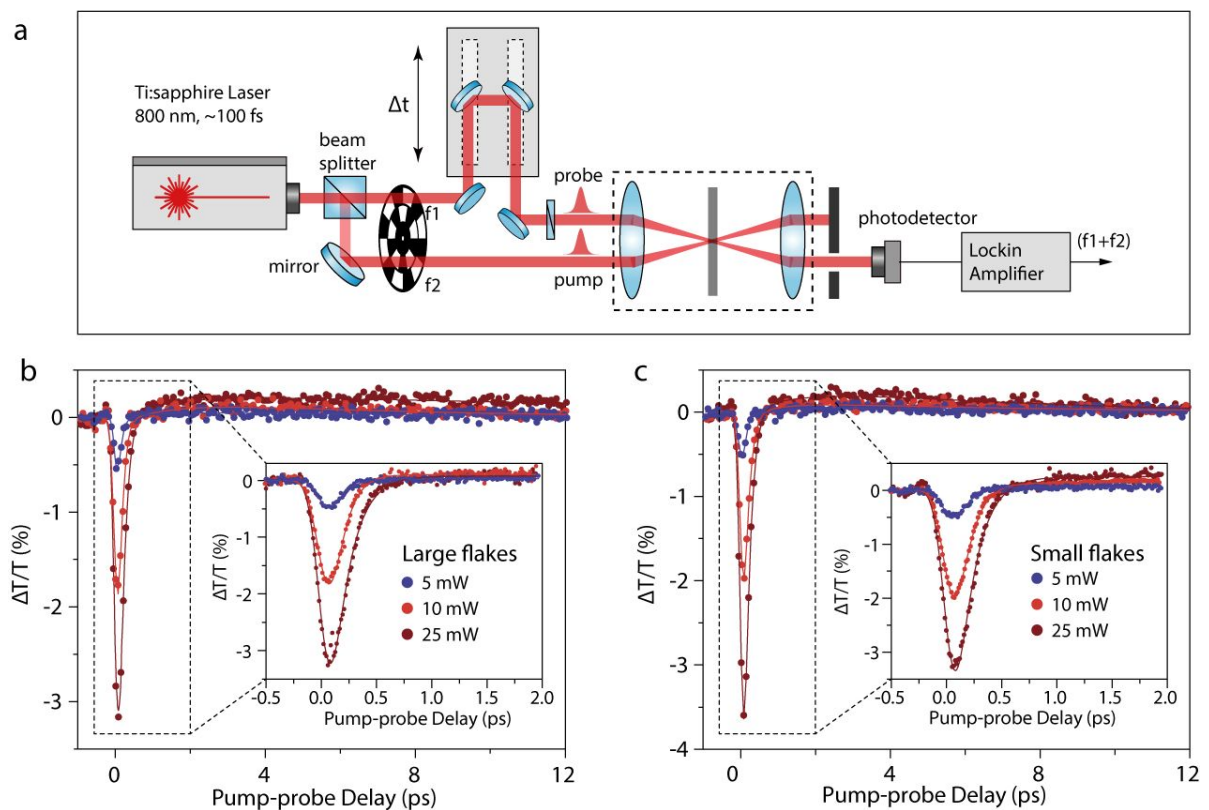

Figure 5 | Time-resolved absorptions of MXene monolayers. a, Schematic of the wavelength-degenerate pump-probe setup based on an 800 nm, 100 fs laser. **b-c,** the experimental time-resolved absorptions of MXene monolayers with large (b) and small (c)

flakes. Solid lines show the fitted curves using a tri-exponential decay model. The insets are the corresponding curves obtained at a relatively short pump-probe decay time from -0.7 ps to 2 ps.
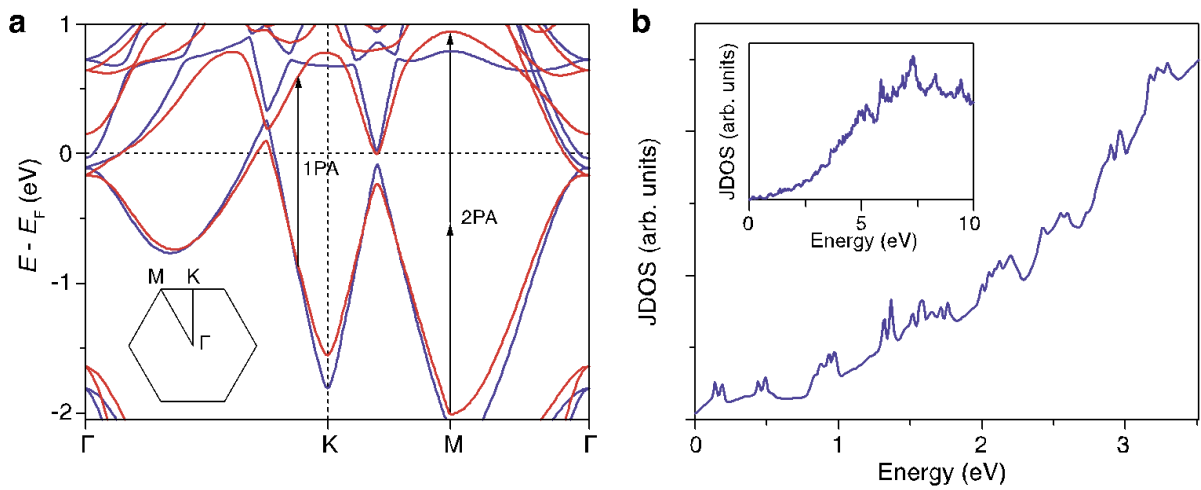

Figure 6 | The calculated electronic properties of MXene monolayers (Ti$_3$C$_2$T$_x$, T = F or OH). **a,** The calculated electronic band structure of monolayer Ti$_3$C$_2$T$_x$. Ti$_3$C$_2$F$_2$ is shown in blue and Ti$_3$C$_2$(OH)$_2$ is shown in red. **b,** Joint density of states (JDOS) as a function of excited photon energy. The inset shows a wide excited photon energy ranging from 0 to 10 eV.

Table 1 | The nonlinear optical properties of the large and small MXene monolayers. These properties are obtained from the fitting of Z-scan measurements.

Sample	Energy	β (cm/GW, ×10^{-2})	Im $\chi^{(3)}$ (esu, ×10^{-14})	FOM (esu cm, ×10^{-15})	$\sigma(\lambda)$ (10^{-2} GW)
Large flakes	100 nJ	1.38 ± 0.25	2.45 ± 0.43	4.00 ± 0.70	1.10 ± 0.19
	200 nJ	1.27 ± 0.23	2.26 ± 0.40	3.70 ± 0.65	1.02 ± 0.18
	300 nJ	0. 95 ± 0.17	1.70 ± 0.30	2.78 ± 0.49	0.77 ± 0.18
Average	--	1.20 ± 0.22	2.14 ± 0.38	3.49 ± 0.61	0.96 ± 0.17
Small flakes	100 nJ	1.10 ± 0.24	1.95 ± 0.42	2.44 ± 0.53	0.77 ± 0.11
	200 nJ	0.86 ± 0.19	1.52 ± 0.33	1.90 ± 0.41	0.67 ± 0.10
	300 nJ	0.71 ± 0.16	1.27 ± 0.27	1.58 ± 0.34	0.57 ± 0.09
Average	---	0.89 ± 0.20	1.58 ± 0.34	1.97 ± 0.43	0.67 ± 0.10

Table 2 | The ultrafast dynamics in MXene monolayers. These results are obtained from the fitting of the pump-probe experiments using Eq. 6.

Flake size	Power	τ_1 (ps)	τ_2 (ps)	τ_3 (ps)	δ (fs)
Large	5 mW	0.09 ± 0.01	0.70 ± 0.12	10.51 ± 1.74	69 ± 11
	15 mW	0.09 ± 0.03	1.33 ± 0.44	6.04 ± 1.99	88 ± 29
	25 mW	0.15 ± 0.02	2.65 ± 0.32	16.53 ± 2.02	81 ± 10
	Average	0.11 ± 0.02	1.56 ± 0.29	11.03 ± 1.92	79 ± 17
Small	5 mW	0.11 ± 0.02	2.56 ± 0.58	5.89 ± 1.34	88 ± 20
	15 mW	0.12 ± 0.002	0.83 ± 0.02	6.80 ± 0.14	86 ± 2
	25 mW	0.14 ± 0.02	1.66 ± 0.24	5.25 ± 0.85	85 ± 12
	Average	0.13 ± 0.02	1.68 ± 0.28	5.98 ± 0.78	86 ± 11